

# Simulating terahertz quantum cascade lasers: Trends from samples from different labs

David O. Winge,<sup>1, a)</sup> Martin Franckić,<sup>1</sup> and Andreas Wacker<sup>1</sup>

*Mathematical Physics, Lund University, Box 118, 22100 Lund, Sweden*

(Dated: 1 September 2016)

We present a systematic comparison of the results from our non-equilibrium Green's function formalism with a large number of AlGaAs-GaAs terahertz quantum cascade lasers previously published in the literature. Employing identical material and simulation parameters for all samples, we observe that discrepancies between measured and calculated peak currents are similar for samples from a given group. This suggests that the differences between experiment and theory are partly due to a lacking reproducibility for devices fabricated at different laboratories. Varying the interface roughness height for different devices, we find that the peak current under lasing operation hardly changes, so that differences in interface quality appear not to be the sole reason for the lacking reproducibility.

PACS numbers: 72.10.-d, 72.20.Ht

## I. INTRODUCTION

Since the first realization of the terahertz (THz) quantum cascade laser<sup>1</sup> (QCL) it has now been shown to be a reliable source of terahertz radiation, although at low temperatures<sup>2</sup>. Different designs have been proposed and fabricated at many different laboratories of the world. Simultaneously, simulations have been performed for a large variety of samples with different models. These can be based on rate equations for the electron densities<sup>3,4</sup>, Monte-Carlo simulations of the Boltzmann equation for the occupations of the k-states in the individual subbands<sup>5-8</sup>, density matrix calculations<sup>9-13</sup>, which have been also done k-resolved<sup>7,14,15</sup>, as well as nonequilibrium Green's functions (NEGF)<sup>16-20</sup>. While the published results from either scheme typically agree well with experimental data, it is not clear how the choices of parameters (in particular interface roughness (IFR) distributions and band offsets), specific approximations (such as screening models or various model-specific assumptions as subband temperatures), or model complexity affects the results.

Therefore we performed simulations with our NEGF scheme<sup>21</sup> for a wide range of different published THz QCLs using precisely the same parameters and model approach, and document *all* results in this paper. This allows to monitor the quality of our simulation scheme. Furthermore, the comparison between devices from different groups can reflect systematic trends. Here it is well-known, that the reproduction of devices from different groups frequently provided different results, where the origin is far from understood, see, e.g., Ref. 22. It is also known that samples grown at the same lab but under different growth campaigns can differ, although methods now exist to guarantee run-to-run reproducibility<sup>23</sup>. The identification of trends in published samples from differ-

ent labs may shine light into discrepancies of the growth procedures, and to pose the right questions for the community to take steps towards inter-lab reproducibility of THz QCL devices.

## II. MODEL AND ESTIMATES

One of the most important parameter in heterostructure modeling is the conduction band offset (CBO), a function of the bandgap of the alloys in question and the valence band offset (VBO). In this work we limit ourselves to  $\text{Al}_x\text{Ga}_{1-x}\text{As}/\text{GaAs}$  systems in the direct bandgap regime. Consulting the standard literature, Vurgaftman *et al.*<sup>24</sup> provides the relation  $\text{CBO} = 0.97x$  eV (in the vicinity of 15% Al content; the full expression is a cubic polynomial in  $x$ ) for  $\text{Al}_x\text{Ga}_{1-x}\text{As}$  barriers. This is in turn based on a VBO of  $0.53x$  eV, assumed temperature independent, as well as low temperature results for the band gaps of both GaAs and AlAs. This relation for the conduction band offset is however seldom used in the QCL community<sup>22,25,26</sup>, where instead a lower offset is often preferred. This might be more reasonable for the design of structures aimed at high temperature operation, where we expect the band gap to decrease. More recent experiments by Yi *et al.*<sup>27</sup> and Lao & Perere<sup>28</sup> have found low temperature VBOs of  $\sim 0.570x$  eV, which would distribute more offset to the valence band side, effectively lowering the CBO. This justifies the use of a lower value compared to Vurgaftman *et al.*. In total, Yi *et al.* found a CBO of  $0.831x$  eV for  $x \leq 0.42$ , at 4.2 K. As the focus of this study is the performance of THz QCL at low temperatures, we will use this result for the CBO in the remainder of this work. Furthermore we use the effective mass of the conduction band edge  $m_{eff} = 0.067 + 0.083x$ , as given in Vurgaftman *et al.*<sup>24</sup> and used by most groups. Together with standard material parameters for bulk GaAs, this defines the heterostructure apart from the doping density and layer sequence. The basis states are then calculated

<sup>a)</sup> Electronic mail: David.Winge@teorfys.lu.se

in an effective two band model<sup>29,30</sup> using a Kane energy of  $E_P = 22.7$  eV<sup>31</sup>.

In our transport model we calculate the scattering self-energies in the self-consistent Born approximation. For the structures of interest, the elastic processes are dominated by impurity and IFR scattering. In addition we include alloy scattering to the elastic self-energies. For modeling IFR we use an exponential correlation function in this work. Gaussian correlation functions have been shown to yield similar results<sup>30</sup>, and the values used here, 0.2/10.0 nm for rms height/correlation length can best be compared to 0.2/7.0 nm for a Gaussian correlation function. Here the use of an effective two band model decreases the impact of the IFR scattering<sup>30</sup>.

In their complete theoretical formulation, the self energies of the NEGF models are functions of both momentum and energy, but in our implementation they are effectively treated as only energy dependent. This is done by evaluating the scattering matrix elements at a set of representative momentum transfers<sup>21</sup>, and reduces the computational effort to an accessible level. Throughout this work we use the typical momentum transfers  $k_0$  equivalent to  $E_k^0 = 6.3$  meV for intra-subband scattering at 77 K lattice temperature. For intersubband scattering, we also adjust for the difference in subband energy. One problem with this procedure is that it introduces a logarithmic divergence in the real parts of the self-energies for increasing  $k$ -ranges covered. The choice of typical momentum transfers and our solution to the problem of the divergence is discussed in detail in Appendix A.

For the inelastic self-energies we include both acoustic and longitudinal optical (LO) phonon scattering. Electron-electron scattering is also implemented via a rudimentary form of the GW approximation<sup>32</sup>, where the screening function is replaced by its plasmon pole. This allows us to go beyond the meanfield approximation and to estimate in which type of structures this mechanism is of importance. The modeling is based on energy exchange of the conduction band electrons with a plasmon bath, with a temperature equal to an effective electron temperature, in order not to artificially cool the electron gas. In Appendix B we discuss how this temperature can be chosen by balancing the electric power dissipated in the structure and the cooling rate of the LO phonons.

### III. SAMPLES STUDIED

In the following, we present a short overview of each class of designs included in this work, and introduce and label each device. They will be referenced in the text by a shorthand notation containing first author name, journal and year, e.g. DupontJAP2012 for the device considered in Ref. 33.

#### A. 2-well designs

The 2-well design is the simplest possible realization of a QCL, which next to the upper and lower laser level employs one further level, serving both for extraction from the lower laser level (by LO phonon scattering) and injection by resonant tunneling (RT) into the upper laser level of the next period. Here we study the first realized structure KumarAPL2009B<sup>34</sup> as well as the broadband laser ScallariOE2010<sup>35</sup>. Both lasers were processed with metal-metal (MM) waveguides and the latter showed high power output when parts of the upper metal contact was removed.

#### B. 3-well designs

The 3-well structures apply an additional well for extraction and thus employ a RT LO phonon depletion mechanism for emptying the lower laser state<sup>36</sup>. This type of design has achieved high operation temperatures with a record temperature achieved in 2012<sup>37</sup>. Variants have been realized in all labs included in this study, except ETH. This fact and the simple layer sequence strategy makes it a very interesting type of design when we want to compare samples of different origin. The lasers studied here are FatholoulumiOE2012<sup>37</sup>, sample V812 of FatholoulumiJAP2013<sup>38</sup>, KumarAPL2009A<sup>39</sup>, DeutschAPL2013<sup>40</sup> and SalihJAP2013<sup>41</sup>. The designs are similar in principle, with small changes in doping densities and oscillator strengths. Despite this similarity, the reported output powers differ drastically depending on both origin and growth campaign as seen in TAB. I. This is most probably due to the procedure of removing parts of the top contact layer of KumarAPL2009A and FatholoulumiOE2012, a procedure described in Ref. 42, which reduces waveguide losses for these samples.

#### C. Hybrid designs

The class of structures that we will denote as *hybrid* borrows ideas both from the bound to continuum structures, which were the first to lase in this spectral range<sup>1</sup>, and the 3-well concept. In these structures a fourth well is inserted, and extraction from the lower laser state to the extractor state occurs through a combination of scattering and RT. Here we study two subclasses of this design type. In the designs BurghoffAPL2011<sup>43</sup>, MartiOE2011<sup>44</sup> and BenzAPL2007<sup>45</sup> a two well injector is used, similar to the pioneering design of Ref. 36, whereas the other samples use RT injection directly from the ground state of the phonon well into the upper laser state as proposed in Ref. 46. Showing good scaling properties, the latter designs are suitable for high power operation<sup>47</sup>, and the robustness in layer sequence can be utilized for broadband multi-stack devices<sup>48</sup>. Here, these designs are labeled as LiEL2014<sup>47</sup>, AmantiNJP2009<sup>46</sup>

and TurcinkovaAPL2011<sup>48</sup>, respectively. As the layer sequence of stack A in Ref. 48 is identical to sample EV1157 of Ref. 46, we compare here to results of the high doped version, labeled N907, when we refer to AmantiNJP2009.

#### D. Indirectly pumped designs

We have also studied the indirectly pumped, also known as scattering assisted injection<sup>49</sup> and phonon-photon-phonon (3P) designs<sup>33</sup>. These designs use LO phonon scattering to populate the upper laser state, which is fundamentally different to the RT injection but requires a larger bias to operate. Here we present results for DupontJAP2012<sup>33</sup>, RazavipourJAP2013<sup>50</sup> and KhanalOE2015<sup>51</sup>.

### IV. PROCEDURE

For each device, we performed simulations based on the nominal sample parameters as listed in each publication. The input parameters are the reported sheet doping densities and layer sequences, whereas the roughness and all other scattering parameters were kept the same (For comparison of the intensity inside the waveguide, also the sample facet area was read out). We use 77 K as lattice temperature in all simulations and compare to experimental data taken in pulsed mode operation, at heat-sink temperatures close to 77 K when possible, or at lower temperatures otherwise. Usually, the experimental data do not show any significant variations in this temperature range.

The main results are collected in TAB. I together with some basic data of the devices, such as the sheet doping density per period  $n_{2D}$  and the reported lasing frequency. Most importantly, we provide the experimental peak current density  $J_{\text{exp}}^{\text{peak}}$  under laser operation for low temperatures, which is the key quantity for comparison, and also the threshold current  $J_{\text{exp}}^{\text{thr}}$ . For comparison, we provide the  $J_{\text{sim}}^{\text{thr}}$ , where the simulated gain reached the threshold value, and the peak current  $J_{\text{sim}}^{\text{dc}}$  of our simulations neglecting the ac field of lasing operation.

A key parameter for the simulation is the threshold gain  $g_{\text{th}}$  in the heterostructure required to overcome waveguide and mirror losses. For the MM waveguides operating around 2 THz we use  $g_{\text{th}} = 10/\text{cm}$ . This roughly corresponds to the electric field losses (which are half the intensity loss used here) of 4.3/cm addressed in Ref. 44. For frequencies above 2.7 THz we use  $g_{\text{th}} = 15/\text{cm}$  and above 3.8 THz we use  $g_{\text{th}} = 20/\text{cm}$  for the MM waveguides, taking into account the higher attenuation in the metals. The device TurcinkovaAPL2011 is a multi-stack design, and as each stack has a significantly smaller mode confinement factor compared to standard devices, we use the enhanced value of  $g_{\text{th}} = 45/\text{cm}$ . For the semi-insulating surface-plasmon (SI-SP) waveguide in LiEL2014, we use  $g_{\text{th}} = 40/\text{cm}$  guided by results given

in Ref. 52. For the second SI-SP waveguide sample SalihJAP2013, we use  $g_{\text{th}} = 100/\text{cm}$  based on the calculated waveguide losses in the publication for a 6  $\mu\text{m}$  wide active region. Note that the free carrier loss in the active region itself is taken into account in the NEGF simulations of the gain spectra.

The response of the active region under operation is simulated using a classical ac field with increasing strength until gain is saturated to the threshold value. This provides an increased peak current  $J_{\text{sim}}^{\text{lase}}$ . The ac field strength is then related to the intensity inside the active region  $I_{\text{sim}}$  via the Poynting vector. The corresponding experimental value  $I_{\text{exp}}$  is obtained from the measured power output at low temperature and pulsed mode operation in the following way: The power is divided by a typical collection efficiency of 30%<sup>42,53,54</sup> and the transmittivity leaving the waveguide, multiplied with the confinement factor of the waveguide, and finally divided by the cross section of the active region. For the transmittivity we use 0.25, 0.20 and 0.15 for the MM waveguides with  $g_{\text{th}}$  of 20, 15 and 10 per cm, respectively, guided by the results of Ref. 52. For the SI-SP waveguides we use a transmittivity of 0.68 calculated from the Fresnel equations. We use unity confinement factors for the MM waveguides, 0.4 for the waveguide of LiEL2014<sup>55</sup> and 0.2 for the waveguide in SalihJAP2013<sup>41</sup>. In this context we note, that the gain saturation, defining the simulated intensity  $I_{\text{sim}}$  contains backwards traveling waves, which do not contribute to the experimental output as discussed in Ref. 56. Thus,  $I_{\text{sim}}$  is expected to overestimate the output by a factor up to two for low transmittivity<sup>57</sup>. These considerations show, that the values of  $I_{\text{exp}}$  can only be seen as rough estimates, where a large part of the uncertainty is due to the collection efficiency.

As an example for our simulations, we show more detailed results for the hybrid design of LiEL2014<sup>47</sup> in FIG. 1. The dc calculations without the ac field (full blue line) exhibit a peak current density  $J_{\text{sim}}^{\text{dc}} = 500 \text{ A/cm}^2$ , and this value is presented in the sixth column of TAB. I. Then we consider the spectral gain for different biases as shown in FIG. 2 in order to determine the threshold current  $J_{\text{sim}}^{\text{thr}}$ , where the material gain surpasses the threshold gain  $g_{\text{th}}$  (if this operation point is in a region of negative differential conductivity, we assume that the threshold occurs in a domain state and use the current density of the preceding peak). Above the threshold current, we perform simulations in the presence of the ac field in order to study the operating device. Here we increase the ac field until gain saturation reduces the gain to  $g_{\text{th}}$ . This provides the light-current-voltage (LIV) characteristics shown in FIG. 1 by a red line with crosses. The maximum current achieved is denoted by  $J_{\text{sim}}^{\text{lase}}$  (here 1100  $\text{A/cm}^2$ ) and this value is presented in the seventh column of TAB. I. In the same way we obtain the intensity  $I_{\text{sim}}$  displayed in the tenth column of TAB. I. In order to judge the relevance of electron-electron scattering, we performed simulations with our plasmon-pole approximation for the off state, as shown by the orange

Type	Ref.	$J_{\text{exp}}^{\text{thr}}$	$J_{\text{sim}}^{\text{thr}}$	$J_{\text{exp}}^{\text{peak}}$	$J_{\text{sim}}^{\text{dc}}$	$J_{\text{sim}}^{\text{lase}}$	$J_{\text{sim}}^{\text{GW dc}}$	$I_{\text{exp}}$	$I_{\text{sim}}$	$\nu_{\text{exp}}$	$n_{2D}$	$g_{th}$	Origin
2-well	KumarAPL2009B <sup>34</sup>	415	510*	950	1040	1700	1100	–	2200	4.5	2.2	20	Sandia
	ScalariOE2010 <sup>35</sup>	470	440	800	520	780*	530	290	790	3.2	1.5	15	ETH
3-well	KumarAPL2009A <sup>39</sup>	440	500	850	610	1860	920	580	1460	3.9	3.0	20	Sandia
	SalihJAP2013 <sup>41</sup>	1300	1050*	1400	1300	1300	1500	0.5	22	3.2	2.75	100	Leeds
	FatholoulumiOE2012 <sup>37</sup>	1000	1200	1600	1350	2120	1800	275	1260	2.7	3.0	15	Ottawa
	FatholoulumiJAP2013 <sup>38</sup>	660	715	1000	900	1490	1270	60	1240	3.3	3.0	15	Ottawa
	DeutschAPL2013 <sup>40</sup>	900	690	1400	850	1230	1075	70	940	3.8	3.3	20	Vienna
Hybrid	BurghoffAPL2011 <sup>43</sup>	360	670	420	760	970	1030	–	790	2.2	3.0	10	Sandia
	LiEL2014 <sup>47</sup>	520	470	700	500	1100	1240	250	340	3.4	5.2	40	Leeds
	AmantiNJP2009 <sup>46</sup>	450	680	810	740	1045	1250	20	470	3.0	11	15	ETH
	TurcinkovaAPL2011 <sup>48</sup>	300	215	430	225	500	670	50	220	3.0	3.7	45	ETH
	BenzAPL2007 <sup>45</sup>	510	450	820	590	770	540	–	385	2.8	1.9	15	Vienna
	MartlOE2011 <sup>44</sup>	165	125*	215	145	170*	170	–	130	2.1	0.6	10	Vienna
Indirect	KhanalOE2015 <sup>51</sup>	800	500*	1350	850	900	740	130	460	2.1	3.17	10	Sandia
	DupontJAP2012 <sup>33</sup>	1250	–	1600	1800	–	2000	10	0	3.0	3.25	15	Ottawa
	RazavipourJAP2013 <sup>50</sup>	850	1100*	1300	1490	1360	1600	85	1300	2.4	3.45	10	Ottawa

TABLE I. Collected simulation results together with the most relevant experimental measurements, grouped with respect to design and origin. Current densities denoted by  $J$  are given in  $\text{A}/\text{cm}^2$ , measured frequencies  $\nu_{\text{exp}}$  in THz, sheet doping densities  $n_{2D}$  in  $10^{10} \text{ cm}^{-2}$  and threshold gain  $g_{th}$  in  $1/\text{cm}$ . Calculated currents showing a particular large sensitivity to the value  $g_{th}$  are marked by asterisks. The simulated lasing intensity within the active region  $I_{\text{sim}}$  has units  $[\mu\text{W}/\mu\text{m}^2]$ . The experimental counterpart  $I_{\text{exp}}$  is based on an estimated collection efficiency of 30% of the reported power at low temperature pulsed operation. A graphical display of the results is found in FIG. 4.

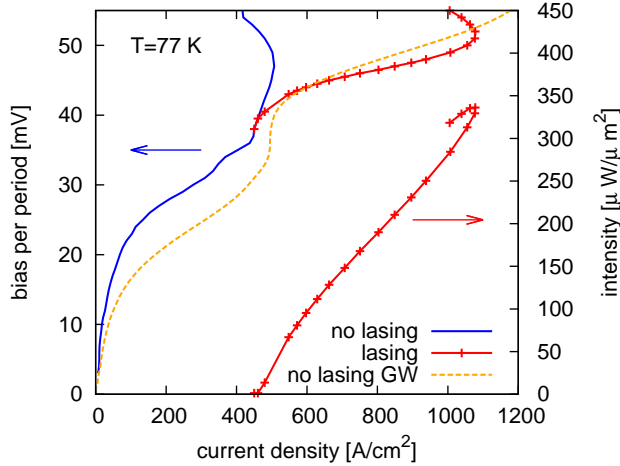


FIG. 1. Light-current-voltage (LIV) characteristics of the 1 W THz QCL presented in Ref. 47 (LiEL2014). The solid blue line indicate the current without lasing, while the crossed red lines show current and intensity under operation. The dashed orange line refers to the simulations taking into account electron-electron scattering in the plasmon-pole approximation.

dashed line in FIG. 1. The corresponding peak current is denoted as  $J_{\text{sim}}^{\text{GW dc}}$ .

Now we discuss the specific results for the sample LiEL2014<sup>47</sup> in more detail: Around the bias matching the optical phonon energy of  $\sim 36 \text{ meV}$  the parasitic

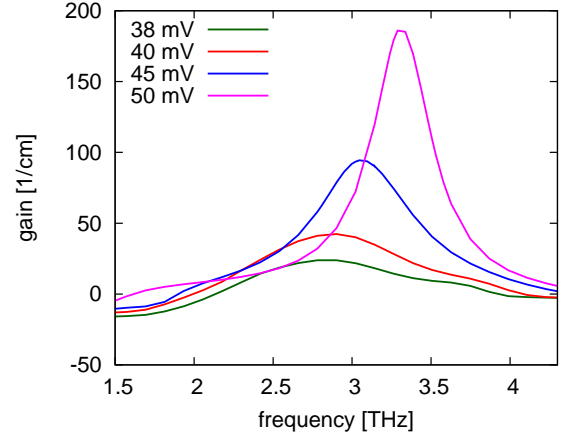


FIG. 2. Gain simulations at a number of different bias points corresponding to the LIV in FIG. 1. A Stark shift can be observed with increasing bias. Experimentally lasing was reported around 3.4 THz<sup>47</sup>.

injection channel is enhanced and seen to give a small feature in the current. After this, the upper laser state is instead favored by the tunneling transition, and inversion is building up, allowing for laser action to start provided the losses are low enough. With no lasing in the cavity, the peak current saturates at  $500 \text{ A}/\text{cm}^2$  before the design bias of 50 mV is reached. The situation is displayed in FIG. 3 where the electron densities are resolved in energy and growth direction. Inversion is clearly visible,



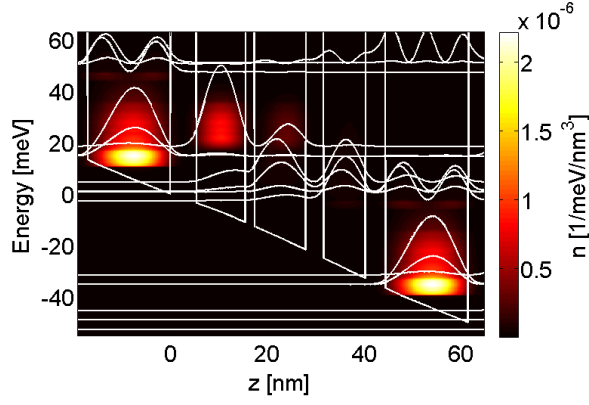


FIG. 3. Energy resolved densities calculated from the lesser Green's function showing how the populations are distributed at the design bias of 50 mV per period, without any laser field included. The inversion between the upper and lower laser state is clearly visualized.

but without laser field the electrons stay relatively long in the injector and upper laser state. When the structure is modeled with a laser field, current is enhanced and the negative differential resistance (NDR) feature is shifted to 52 mV, allowing the structure to reach its intended configuration. From the GW results in FIG. 1 we see also that the inelastic scattering from electron-electron interactions can enhance the charge transfer through the structure.

Assuming losses of 40/cm, the threshold current is 470 A/cm<sup>2</sup>, which is in reasonable agreement with the experimental value at 400 A/cm<sup>2</sup>. The calculated dynamical range however, can be seen to exceed 600 A/cm<sup>2</sup> which is a factor of two larger than what is seen experimentally. Simultaneously, the calculated intensity  $I_{\text{sim}}$  is slightly above the experimental value  $I_{\text{exp}}$ . Here we also note, that we assume a homogeneous field ac and dc field in the heterostructure region of the sample. While this is well-justified for the dc-field, the actual ac-field-distribution depends on the waveguide. In particular for SI-SP waveguides, the ac-field is not homogeneous in the growth direction, which is disregarded by our scheme. Thus we are not surprised, that our approach overestimates both the simulated peak current  $J_{\text{sim}}^{\text{lase}}$  and intensity  $I_{\text{sim}}$ .

## V. RESULTS

Collected results from all simulations are shown in TAB. I together with relevant experimental quantities. In the following, we focus on the maximum current under operation and the threshold current, which are most easily extractable for the experimental data. (Only two samples, SalihJAP2013 and MartlOE2011, did not show a clear NDR feature after maximum power in their respective reference, which adds some uncertainty in their respective  $J_{\text{exp}}^{\text{peak}}$ .) As the assumption of homogeneous ac-fields tends to overestimate the lasing intensity, we would

expect this experimental peak current to be between  $J_{\text{sim}}^{\text{dc}}$  and  $J_{\text{sim}}^{\text{lase}}$ . If  $J_{\text{sim}}^{\text{GW dc}}$  is much larger than  $J_{\text{sim}}^{\text{dc}}$ , electron-electron scattering appears to be more important, so that the other calculated currents may be too low.

In most of our simulations, the peak current is a slowly varying function of the losses once high intensity is reached, which reduces the impact of an erroneous estimate of  $g_{\text{th}}$ . On the other hand, the threshold current can be very sensitive to this parameter. For samples where we find that the currents are very sensitive to the value of  $g_{\text{th}}$ , we mark the relevant quantity with an asterisk in TAB. I.

The ratios  $J_{\text{sim}}^{\text{dc}}/J_{\text{exp}}^{\text{peak}}$ ,  $J_{\text{sim}}^{\text{lase}}/J_{\text{exp}}^{\text{peak}}$ ,  $J_{\text{sim}}^{\text{GW dc}}/J_{\text{exp}}^{\text{peak}}$ , and  $J_{\text{sim}}^{\text{thr}}/J_{\text{exp}}^{\text{thr}}$  are displayed in FIG. 4(a) for an easy identification of the overall quality of the simulations. As in TAB. I, the samples are ordered according to the design class. We find, that the model provides good results for many samples, but within each design class there are devices, where the experimental and calculated currents disagree significantly. Furthermore, we find, that  $J_{\text{sim}}^{\text{GW dc}}$  does not differ much from  $J_{\text{sim}}^{\text{dc}}$  except for several hybrid designs, such as LiEL2014 discussed above.

In order to study, why the simulations appear to describe some devices better than others, we now order the results in different ways. First, we order the devices according to the measured intensity, which could reveal problems of our model to describe the devices under operation. However, FIG. 4 (b) shows no clear trend. Secondly, we order the devices according to the doping intensity, which is relevant for impurity scattering and electron-electron scattering. Again, FIG. 4 (c) does not provide any trend for the reliability of our model (samples with sheet doping density of  $3 \cdot 10^{10}/\text{cm}^2$  are shaded as a guidance). However, we note, that for high doping density  $J_{\text{sim}}^{\text{GW dc}}$  becomes much larger than  $J_{\text{sim}}^{\text{dc}}$  indicating the relevance of electron-electron scattering. Thirdly, we sort the devices with respect to growth place in FIG. 4(d). Here we find a clear trend, where the simulations with the parameters mentioned above provide too low currents for the devices grown at the Technical University of Vienna and too high currents for devices grown at Sandia (except for KhanalOE2015, which we discuss below). For samples grown at the NRC in Ottawa and in Leeds, our model provides good agreement with the experimental peak current and threshold current. For samples grown at ETH, the results are slightly more scattered. In particular the calculated  $J_{\text{sim}}^{\text{thr}}$  for AmantiNJP2009 is too large.

The rightmost device in FIG. 4(d) KhanalOE2015, an indirect design, does not fit the picture. While the indirect designs have barriers with  $x = 0.25$ , this device has a lower barrier height ( $x = 0.15$ ), which may provide substantial leakage into the continuum<sup>22</sup> for the high electric field required for indirect designs. This is not taken into account in the NEGF model and could explain, why the model provides a smaller peak current. To explore this hypothesis, we have studied the parasitic resonances where they cause an experimental NDR feature, visible as a distinguished pre-

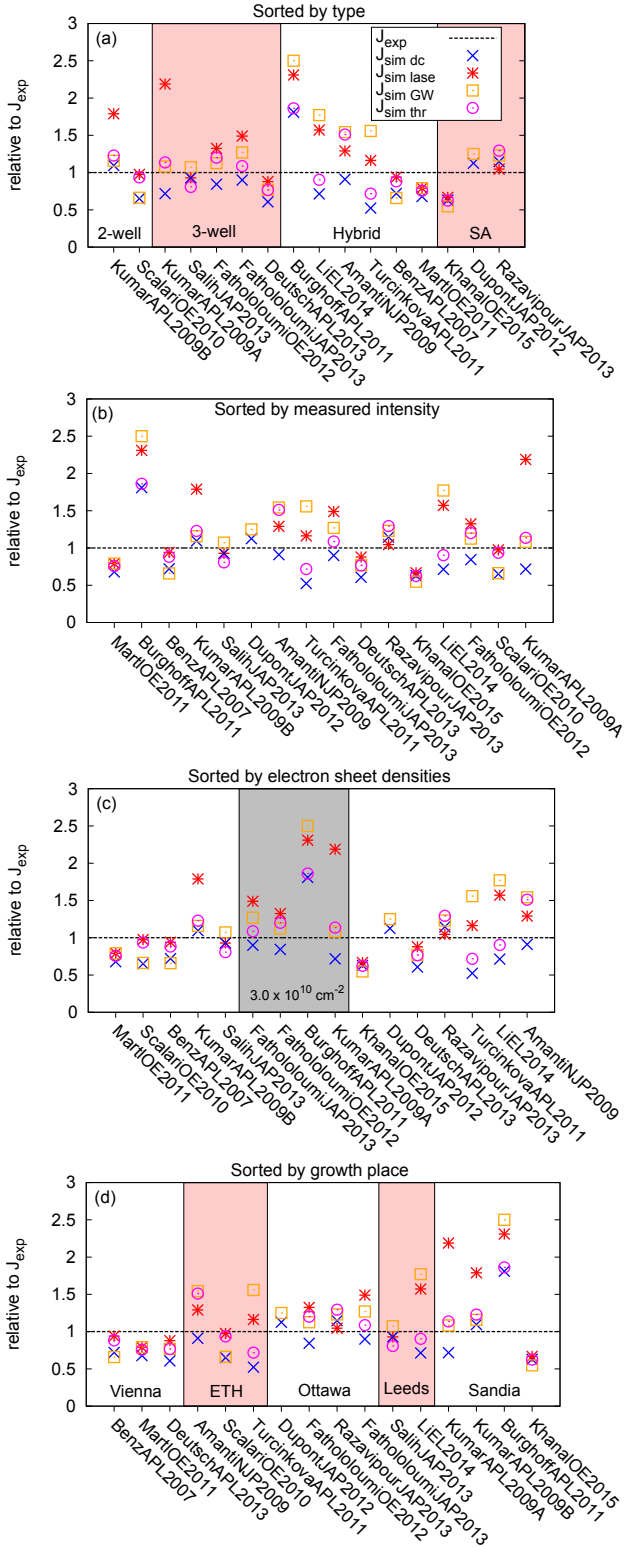


FIG. 4. Simulated currents divided by experimental currents. The panels order the samples according to (a) design class as in TAB. I, (b) from low (left) to high (right) experimental lasing intensity, (c) from low (left) to high (right) sheet doping density, and in (d), samples from the same lab have been grouped together.

peak in the LIV. This is true for all studied samples of the indirect class, and also for KumarAPL2009A, KumarAPL2009B, FatholouloumiOE2012, DeutschAPL2013 and FatholouloumiJAP2013. For the samples from Sandia, including KhanalOE2015, we overestimate the pre-peak currents by more than 25% in all cases, while we have agreement within 20% for the other samples. Thus, the currents at the parasitic resonances agree with the main trend of FIG. 4(d), that we overestimate the currents of the Sandia devices.

In addition we compare simulated and measured intensity for each sample. The procedure is described in Sec. II, and experimental values, when available, are listed in TAB. I. For all structures studied, we overestimate the waveguide intensity. For the sample LiEL2014, utilizing a SI-SP waveguide, we get rather good agreement between our calculations and the experimental data. Assuming, that backwards traveling waves correspond to half the calculated intensity in the MM waveguides of ScalariOE2010, KumarAPL2009A, KhanalOE2015, the discrepancy is reduced to less than 50%. The other samples show even lower measured intensity, which we cannot explain here. Possible causes could be the overestimation of the simulated intensity due to simplified model assumptions such as the neglect of heated phonons<sup>58,59</sup>, uncertainties in parameters such as threshold gain and transmittivity, an experimental collection efficiency far below  $\sim 30\%$ , or non-uniformity of the laser field in the cavity.

## VI. SENSITIVITY OF GROWTH PARAMETERS

The trends observed for samples from different groups indicates, that samples grown from same the design at different places are not identical. Likely reasons are deviations in doping, the Al content  $x$ , as well as different IFR. In our simulations we normally observe a linear increase in current with doping, although the same trivial dependence does not hold for gain<sup>20,60</sup>. As the dependence on IFR and Al content are not equally well understood, we have conducted several numerical experiments to estimate the impact of fluctuations in these parameters.

By increasing the barrier height we expect a decrease in current as the tunneling amplitudes decrease. This is indeed what we find, and we show this in FIG. 5(a) where simulations with altered Al content compared to the nominal simulations in FIG. 1 are shown. The linear dependence of both dc and lasing current show few surprises; here decreasing barrier heights of 1% Al gives an increase in current of about 10%. In contrast, the impact of changing the rms roughness height  $\eta$  is more remarkable as shown in FIG. 5(b). Compared to the nominal calculations with  $\eta = 0.2$  we get 50% more dc current when  $\eta$  is doubled. On the other hand, the current under irradiation is almost unchanged. This conservation of current can be understood as two competing mecha-

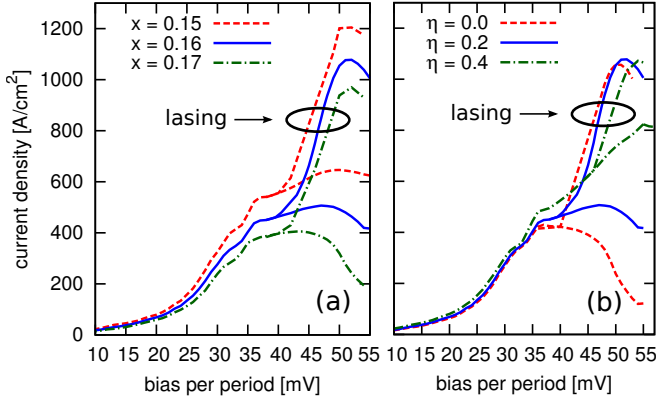


FIG. 5. Sensitivity of currents to varying simulation parameters for the sample LiEL2014<sup>47</sup>. In (a) the Al content  $x$  is changed giving lower and higher barriers for  $x = 0.15$  and  $x = 0.17$  respectively, compared to the nominal one with  $x = 0.16$ . In (b) the IFR height  $\eta$  is changed within two extreme values.

nisms, where either stimulated photon emission or elastic scattering is depleting the upper laser state. The cost of stronger scattering is a smaller dynamic range which will impede higher temperature operation. This analysis suggests two bottlenecks in the transport, the lifetime of the upper laser state and the tunneling rate over the injection barrier.

In order to verify this observation, we performed corresponding simulations with modified IFR for two further structures with different designs as shown in FIG. 6. For KumarAPL2009B, FIG. 6(a) confirms the trend seen for LiEL2014 in FIG. 5(b), that the current under lasing balances the drastic changes seen in the dc current when the roughness parameters are changed. Here the peak current under lasing also shows some sensitivity to the roughness parameters. We believe this to be the coherent part of the injection tunneling current decreasing due to increased scattering. This can explain the loss in total current (incoherent and coherent) under lasing for increasing roughness, as the upper laser state is no longer as efficiently populated. In the case of DupontJAP2012 we see a slight increase at lower biases with increasing scattering, as shown in FIG. 6(b), however at design bias, the current is not significantly effected, and the current at both peaks agrees well with the experimental data. As this laser is depopulated via RT and subsequent resonant phonon scattering<sup>33</sup>, this current bottleneck seems not be very sensitive to additional elastic scattering. These simulations provided gain below 10/cm for all roughness heights at the current peak. However, including our rudimentary electron-electron scattering or raising temperature provides gain slightly above 15/cm, in accordance with the observed weak lasing.

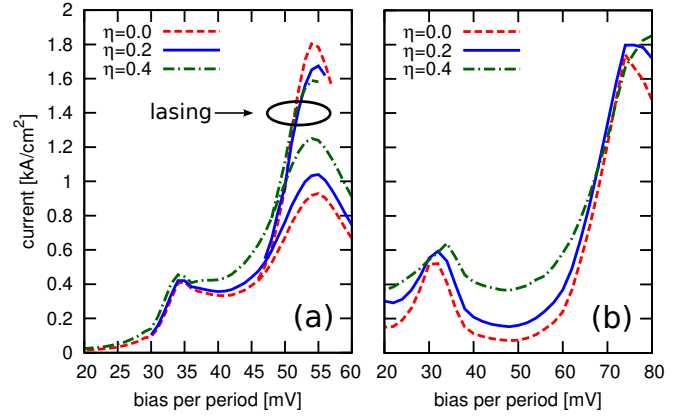


FIG. 6. Simulated current for different IFR heights  $\eta$  for the samples KumarAPL2009B (a) and DupontJAP2012 (b).

## VII. CONCLUSIONS

An extensive study was made including 16 samples among published work on terahertz QCLs from the last ten years, using our NEGF simulation scheme. Using identical simulation parameters, we find that the simulated current does not agree with experimental results for all samples. However, we observe a clear trend that these deviations are similar for samples from a given laboratory. This shows that samples from different laboratories are not fully comparable. We show that interface roughness alone cannot account for these deviations in the simulated current under lasing compared to experimental data. Assuming different calibrations of doping density or Al content in different laboratories could explain these trends. However more intricate issues, such as different barrier profiles, cannot be ruled out.

## ACKNOWLEDGMENTS

We thank K. Unterrainer, G. Strasser, and J. Faist for helpful discussions and the Swedish Research Council for financial support.

## Appendix A: Asymptotic behavior of the self-energies

In the formalism presented in Ref. 21 the elastic self-energies are expressed as

$$\Sigma_{\alpha\alpha'}^{</r}(E, E_k) = \sum_{\beta\beta'} \int_0^\infty dE_{k'} G_{\beta\beta'}^{</r}(E, E_{k'}) \times \underbrace{\frac{\rho_0 A}{4\pi} \int_0^{2\pi} d\varphi \langle V_{\alpha\beta}(E_k, E_{k'}, \varphi) V_{\beta'\alpha'}(E_k, E_{k'}, \varphi) \rangle_{\text{imp}}}_{X_{\alpha\alpha', \beta\beta'}^{\text{elast}}(E_k, E_{k'})} \quad (\text{A1})$$

where  $</r$  denotes the lesser and retarded objects, respectively,  $\rho_0$  is the background density  $em_{eff}m_e/(\pi\hbar^2)$ ,  $A$  is the lateral area and  $V_{\alpha\beta}$  are the scattering matrix elements for each process considered, impurity averaged over all configurations of scattering potentials. The self-energies, being functions of both  $E$  and  $E_k$ , are integrals in  $E_{k'}$  of the Green's function  $G(E, E_{k'})$  and the angle averaged matrix elements  $X_{\alpha\alpha'\beta\beta'}^{\text{elast}}(E_k, E_{k'})$ .

Using the non-interacting Green's function  $G_{\beta\beta}(E, E_{k'}) \sim (E - E_\beta - E_{k'} + i\Gamma)^{-1}$  with a phenomenological broadening  $\Gamma$ , as an approximation, the most interesting parts in the self-energies are found around  $E = E_\beta + E_{k'}$  and at  $E = E_\alpha + E_k$ , where the self-energies peak. This motivates the use of the typical energies  $E_k^0, E_{k'}^0$ , effectively moving the scattering matrix elements out of the integral over  $E_{k'}$  and making the self-energies functions of  $E$  only. To fix  $E_k^0$ , we calculate the intra- and inter-subband scattering rates using thermalized Boltzmann-like subbands at different electron temperatures. This is done for a set of representative low doped heterostructures, and the  $E_k^0$  giving the best agreement for the self-energies to these rates is chosen. From this procedure we find the relation  $E_k^0 = 3.0 \text{ meV} + 0.5 k_B T$  with the lattice temperature  $T$ , used for all simulations presented here. The second typical energy  $E_{k'}^0 = E_k^0 + \Delta E$  is then chosen to reflect the level difference  $\Delta E$  as discussed in Ref. 21.

While the imaginary part of the remaining Green's function vanishes like  $1/E_{k'}^2$  for large values, the real part has a logarithmic divergence, effectively making the self-energies dependent on the  $E_{k'}^{\text{max}}$  chosen in the numerical implementation of Eq. (A1). To remedy this artefact we subtract the part of the integral over a certain critical  $E_k^{\text{cutoff}} = \text{MAX}(E_k^0, E_{k'}^0) + M$  where  $M$  is an appropriate margin. Using the non-interacting Green's function, we express the divergent part as

$$\Sigma_{\alpha\alpha}^{\text{div}}(E) \approx -X_{\alpha\alpha,\beta\beta}^{\text{elast}}(E_k^0, E_{k'}^0) \times \log \left( \frac{E_{k'}^{\text{max}} + E_\beta - E}{E_k^{\text{cutoff}} + E_\beta - E} \right) \quad (\text{A2})$$

where we have restricted us to the diagonal parts of the scattering tensor  $X^{\text{elast}}$ . In order to remove the energy dependence we evaluate the right hand side using a typical energy  $E = E_\alpha + E_k$ . In this work we use  $M = 20 \text{ meV}$  as this was found to give results in good correspondence to fully momentum dependent calculations.

This provides us with a systematic procedure to evaluate and compensate for the artificial divergence in the real parts, and renders the self-energies independent on the integration limits in the implementation, provided a sufficient range is used to cover all relevant physical processes.

## Appendix B: Choosing an effective electron temperature

The electron temperature is by definition an eluding quantity when doing non-equilibrium simulations. In any

model where this thermodynamic intensive property is needed as an input parameter, the difficulties will have to be circumvented in some way. While our standard model evaluates all distribution functions self-consistently and thus does not require this concept at all, we need the electron temperature for the plasmon occupations in the single plasmon-pole approximation used to approximate the GW result<sup>32</sup>.

In the following we will model the conduction band of the quantum cascade laser as one effective band, with an electron temperature  $T_e$  as one of its properties. A bias over this structure will heat the electrons, and they will subsequently relax emitting optical phonons. As the rate at which the electrons cool increases with their temperature, a fixed point is reached. The energy balance must thus fulfill

$$J \cdot (Fd) = en^{2D} E_{\text{LO}} \left( \frac{1}{\langle \tau_{\text{em}} \rangle} - \frac{1}{\langle \tau_{\text{abs}} \rangle} \right) \quad (\text{B1})$$

where  $J$  is the electron current density,  $Fd$  the bias over one period,  $n^{2D}$  the electron sheet density of one period,  $E_{\text{LO}}$  the energy of the longitudinal optical phonon and  $(\tau_{\text{abs/em}})^{-1}$  the rates of emitting or absorbing one such phonon, respectively. Here the scattering times have been averaged over a statistical distribution. Acoustic phonon scattering is assumed to be small, and electron scattering only able to redistribute the carriers according to the electron temperature.

If the rates can be expressed as functions of electron temperature, we can extract this if the current and bias are known. For a bulk system the emission rate from a state with wave-vector  $\mathbf{k}$  is given by

$$\Gamma_{\mathbf{k}} = \frac{C}{(2\pi)^2} \frac{\pi}{\alpha k} \Theta(E_k - E_{\text{LO}}) \log \left| \frac{k + k_0}{k - k_0} \right| \quad (\text{B2})$$

where we have summed over all possible final states. Here,  $k_0 = \sqrt{(E_k - E_{\text{LO}})/\alpha}$  with  $\alpha = \hbar^2/2m_{eff}m_e$  and  $k = |\mathbf{k}|$ . The constant  $C$  is given by

$$C = \frac{(n_{\text{LO}} + 1)}{\hbar} \frac{e^2 E_{\text{LO}}}{2\epsilon_0} \left( \frac{1}{\epsilon(\infty)} - \frac{1}{\epsilon(0)} \right) \quad (\text{B3})$$

with the phonon occupation number  $n_{\text{LO}} = (1 - \exp(E_{\text{LO}}/k_B T_L))^{-1}$ , and the relative permittivities  $\epsilon(0)$  and  $\epsilon(\infty)$  at  $E = 0$  and infinity, respectively.

Averaging over a Maxwell-Boltzmann distribution in 3D we find

$$\frac{\sum_{\mathbf{k}} f_{\mathbf{k}} \Gamma_{\mathbf{k}}}{\sum_{\mathbf{k}} f_{\mathbf{k}}} = \frac{2}{\sqrt{\pi} (k_B T_e)^{3/2}} \times \int_{E_{\text{LO}}}^{\infty} dE_k e^{-\frac{E_k}{k_B T_e}} \frac{C}{4\pi\sqrt{\alpha}} \log \left| \frac{k + k_0}{k - k_0} \right|, \quad (\text{B4})$$

which is now independent of  $\mathbf{k}$  and a function only of electron temperature. In order to get analytical expressions the integrand can be linearized, and this yields the result

$$\frac{\sum_{\mathbf{k}} f_{\mathbf{k}} \Gamma_{\mathbf{k}}}{\sum_{\mathbf{k}} f_{\mathbf{k}}} \approx 2e^{-\frac{E_{\text{LO}}}{k_B T_e}} \frac{C}{4\pi\sqrt{E_{\text{LO}}\alpha}}.$$



for  $\langle\tau_{\text{em}}\rangle^{-1}$  and a similar expression is easily obtained for the absorption process. The scattering times in Eq. (B1) are thus known and solving for electron temperature yields the final result as

$$k_B T_e = \frac{-E_{\text{LO}}}{\log \left[ 2 \frac{J \cdot (Fd)}{n^{2D} C \sqrt{E_{\text{LO}} \alpha}} + e^{-\frac{E_{\text{LO}}}{k_B T_L}} \right]}. \quad (\text{B5})$$

Here the low power limit can be seen as the electron temperature will approach the lattice temperature. As the electric power increases the electron gas is heated. As an example, we find an electron temperature of 130 K for  $Fd = 50$  mV,  $J = 1000$  A/cm<sup>2</sup>,  $n^{2D} = 3.0 \cdot 10^{10}$ /cm<sup>2</sup> and a lattice temperature of 77 K.

- <sup>1</sup>R. Köhler, A. Tredicucci, F. Beltram, H. E. Beere, E. H. Linfield, A. G. Davies, D. A. Ritchie, R. C. Iotti, and F. Rossi, *Nature* **417**, 156 (2002).
- <sup>2</sup>B. S. Williams, *Nat. Photonics* **1**, 517 (2007).
- <sup>3</sup>K. Donovan, P. Harrison, and R. W. Kelsall, *Appl. Phys. Lett.* **75**, 1999 (1999).
- <sup>4</sup>D. Indjin, P. Harrison, R. W. Kelsall, and Z. Ikonik, *J. Appl. Phys.* **91**, 9019 (2002).
- <sup>5</sup>S. Tortora, F. Compagnone, A. Di Carlo, P. Lugli, M. T. Pellegrini, M. Troccoli, and G. Scamarcio, *Physica B* **272**, 219 (1999).
- <sup>6</sup>R. C. Iotti and F. Rossi, *Appl. Phys. Lett.* **78**, 2902 (2001).
- <sup>7</sup>I. Waldmueller, W. W. Chow, E. W. Young, and M. C. Wanke, *IEEE J. Quantum Elect.* **42**, 292 (2006).
- <sup>8</sup>C. Jirauschek, G. Scarpa, P. Lugli, M. S. Vitiello, and G. Scamarcio, *J. Appl. Phys.* **101**, 086109 (2007).
- <sup>9</sup>H. Callebaut and Q. Hu, *J. Appl. Phys.* **98**, 104505 (2005).
- <sup>10</sup>S. Kumar and Q. Hu, *Phys. Rev. B* **80**, 245316 (2009).
- <sup>11</sup>A. Gordon and D. Majer, *Phys. Rev. B* **80**, 195317 (2009).
- <sup>12</sup>E. Dupont, S. Fatholouloumi, and H. C. Liu, *Phys. Rev. B* **81**, 205311 (2010).
- <sup>13</sup>R. Terazzi and J. Faist, *New J. Phys.* **12**, 033045 (2010).
- <sup>14</sup>R. C. Iotti and F. Rossi, *Phys. Rev. Lett.* **87**, 146603 (2001).
- <sup>15</sup>C. Weber, A. Wacker, and A. Knorr, *Phys. Rev. B* **79**, 165322 (2009).
- <sup>16</sup>S.-C. Lee and A. Wacker, *Phys. Rev. B* **66**, 245314 (2002).
- <sup>17</sup>T. Schmielau and M. Pereira, *Appl. Phys. Lett.* **95**, 231111 (2009).
- <sup>18</sup>T. Kubis, C. Yeh, P. Vogl, A. Benz, G. Fasching, and C. Deutsch, *Phys. Rev. B* **79**, 195323 (2009).
- <sup>19</sup>G. Haldas and A. Kolek, and I. Tralle, *IEEE J. Quantum Elect.* **47**, 878 (2011).
- <sup>20</sup>T. Grange, *Phys. Rev. B* **92**, 241306 (2015).
- <sup>21</sup>A. Wacker, M. Lindskog, and D. Winge, *IEEE J. Sel. Top. Quant.* **19**, 1200611 (2013).
- <sup>22</sup>C. W. I. Chan, Q. Hu, and J. L. Reno, *Appl. Phys. Lett.* **103**, 151117 (2013).
- <sup>23</sup>L. H. Li, J. X. Zhu, L. Chen, A. G. Davies, and E. H. Linfield, *Opt. Express* **23**, 2720 (2015).
- <sup>24</sup>I. Vurgaftman, J. R. Meyer, and L. R. Ram-Mohan, *J. Appl. Phys.* **89**, 5815 (2001).
- <sup>25</sup>C. Sirtori, H. Page, C. Becker, and V. Ortiz, *IEEE J. Quantum Elect.* **38**, 547 (2002).
- <sup>26</sup>S. Kumar, *Development of terahertz quantum-cascade lasers*, Ph.D. thesis, Massachusetts Institute of Technology. Dept. of Electrical Engineering and Computer Science (2007).
- <sup>27</sup>W. Yi, V. Narayanamurti, H. Lu, M. A. Scarpulla, and A. C. Gossard, *Phys. Rev. B* **81**, 235325 (2010).
- <sup>28</sup>Y.-F. Lao and A. G. U. Perera, *Phys. Rev. B* **86**, 195315 (2012).
- <sup>29</sup>M. Lindskog, D. O. Winge, and A. Wacker, *Proc. SPIE* **8846**, 884603 (2013).
- <sup>30</sup>M. Franckić, D. O. Winge, J. Wolf, V. Liverini, E. Dupont, V. Trinité, J. Faist, and A. Wacker, *Opt. Express* **23**, 5201 (2015).
- <sup>31</sup>E. O. Kane, *J. Phys. Chem. Solids* **1**, 249 (1957).
- <sup>32</sup>D. O. Winge, M. Franckić, C. Verdozzi, A. Wacker, and M. F. Pereira, *J. Phys.: Conf. Ser.* **696**, 012013 (2016).
- <sup>33</sup>E. Dupont, S. Fatholouloumi, Z. R. Wasilewski, G. Aers, S. R. Laframboise, M. Lindskog, S. G. Razavipour, A. Wacker, D. Ban, and H. C. Liu, *J. Appl. Phys.* **111**, 073111 (2012).
- <sup>34</sup>S. Kumar, C. W. I. Chan, Q. Hu, and J. L. Reno, *Appl. Phys. Lett.* **95**, 141110 (2009).
- <sup>35</sup>G. Scalari, M. I. Amanti, C. Walther, R. Terazzi, M. Beck, and J. Faist, *Opt. Express* **18**, 8043 (2010).
- <sup>36</sup>B. S. Williams, S. Kumar, H. Callebaut, Q. Hu, and J. L. Reno, *Appl. Phys. Lett.* **83**, 5142 (2003).
- <sup>37</sup>S. Fatholouloumi, E. Dupont, C. Chan, Z. Wasilewski, S. Laframboise, D. Ban, A. Mátyás, C. Jirauschek, Q. Hu, and H. C. Liu, *Opt. Express* **20**, 3866 (2012).
- <sup>38</sup>S. Fatholouloumi, E. Dupont, Z. R. Wasilewski, C. W. I. Chan, S. G. Razavipour, S. R. Laframboise, S. Huang, Q. Hu, D. Ban, and H. C. Liu, *J. Appl. Phys.* **113**, 113109 (2013).
- <sup>39</sup>S. Kumar, Q. Hu, and J. L. Reno, *Appl. Phys. Lett.* **94**, 131105 (2009).
- <sup>40</sup>C. Deutsch, H. Detz, M. Krall, M. Brandstetter, T. Zederbauer, A. M. Andrews, W. Schrenk, G. Strasser, and K. Unterrainer, *Appl. Phys. Lett.* **102**, 201102 (2013).
- <sup>41</sup>M. Salih, P. Dean, A. Valavanis, S. P. Khanna, L. H. Li, J. E. Cunningham, A. G. Davies, and E. H. Linfield, *J. Appl. Phys.* **113**, 113110 (2013).
- <sup>42</sup>M. A. Belkin, J. A. Fan, S. Hormoz, F. Capasso, S. P. Khanna, M. Lachab, A. G. Davies, and E. H. Linfield, *Opt. Express* **16**, 3242 (2008).
- <sup>43</sup>D. Burghoff, T.-Y. Kao, D. Ban, A. W. M. Lee, Q. Hu, and J. Reno, *Appl. Phys. Lett.* **98**, 061112 (2011).
- <sup>44</sup>M. Martl, J. Darmo, C. Deutsch, M. Brandstetter, A. M. Andrews, P. Klang, G. Strasser, and K. Unterrainer, *Opt. Express* **19**, 733 (2011).
- <sup>45</sup>A. Benz, G. Fasching, A. M. Andrews, M. Martl, K. Unterrainer, T. Roch, W. Schrenk, S. Golka, and G. Strasser, *Appl. Phys. Lett.* **90**, 101107 (2007).
- <sup>46</sup>M. I. Amanti, G. Scalari, R. Terazzi, M. Fischer, M. Beck, J. Faist, A. Rudra, P. Gallo, and E. Kapon, *New J. Phys.* **11**, 125022 (2009).
- <sup>47</sup>L. Li, L. Chen, J. Zhu, J. Freeman, P. Dean, A. Valavanis, A. G. Davies, and E. H. Linfield, *Electron. Lett.* **50**, 309 (2014).
- <sup>48</sup>D. Turčínková, G. Scalari, F. Castellano, M. I. Amanti, M. Beck, and J. Faist, *Appl. Phys. Lett.* **99**, 191104 (2011).
- <sup>49</sup>S. Kumar, C. W. I. Chan, Q. Hu, and J. L. Reno, *Nat. Physics* **7**, 166 (2011).
- <sup>50</sup>S. G. Razavipour, E. Dupont, S. Fatholouloumi, C. W. I. Chan, M. Lindskog, Z. R. Wasilewski, G. Aers, S. R. Laframboise, A. Wacker, Q. Hu, D. Ban, and H. C. Liu, *J. Appl. Phys.* **113**, 203107 (2013).
- <sup>51</sup>S. Khanal, J. L. Reno, and S. Kumar, *Opt. Express* **23**, 19689 (2015).
- <sup>52</sup>S. Kohen, B. Williams, and Q. Hu, *J. Appl. Phys.* **97**, 053106 (2005).
- <sup>53</sup>L. Ajili, G. Scalari, J. Faist, H. Beere, E. Linfield, D. Ritchie, and G. Davies, *Appl. Phys. Lett.* **85**, 3986 (2004).
- <sup>54</sup>M. S. Vitiello, G. Scamarcio, V. Spagnolo, S. S. Dhillon, and C. Sirtori, *Applied Physics Letters* **90**, 191115 (2007).
- <sup>55</sup>An estimate based on laser frequency, waveguide width and plasma layer thickness guided by Ref. 52.
- <sup>56</sup>D. O. Winge, M. Lindskog, and A. Wacker, *Opt. Express* **22**, 18389 (2014).
- <sup>57</sup>A full calculation is difficult, as standing waves provide an inhomogeneous profile contrary to main simulation assumptions.
- <sup>58</sup>M. S. Vitiello, R. C. Iotti, F. Rossi, L. Mahler, A. Tredicucci, H. E. Beere, D. A. Ritchie, Q. Hu, and G. Scamarcio, *Applied Physics Letters* **100**, 091101 (2012).
- <sup>59</sup>Y. B. Shi and I. Knezevic, *Journal of Applied Physics* **116**, 123105 (2014).
- <sup>60</sup>A. Wacker, *Appl. Phys. Lett.* **97**, 081105 (2010).